DEVELOPING A MULTI-PHASE WELDING SIMULATION WITH DAMAGE PREDICTION SOURCING ON STANDARDIZED TENSILE TESTS AND EXPERIMENTAL VALIDATION BY DAMAGING A WELDMENT

C. SCHRÖDER*, T. LOOSE**, M. BRODT*

**Technologie Institut für Metall und Engineering GmbH, Germany*
***Dr. Loose GmbH, Germany*

DOI 10.3217/978-3-99161-089-2-020, license CC BY 4.0

ABSTRACT

To accurately simulate the strength and potential damage of welded joints in structural steel, a multi-phase welding simulation is required. This is because phase transformations in the heat-affected zone (HAZ) change the local mechanical properties significantly. The main microstructural phases of steel (ferrite/pearlite, bainite, and martensite) exhibit distinct mechanical properties such as tensile strength and fracture elongation. For the prediction of damage in welding seams, these properties play a critical role and must be considered. Welding seams can be simulated with computational welding mechanics (CWM) by calculating stresses, strains, distortions, and microstructural transformations in the HAZ. For the microstructure transformations, the effects on structural properties are considered using multi-phase material models [1], [2]. Such a multi-phase material is developed and implemented in the commercial software LS-DYNA by [3], which is available as keyword ***MAT_GENERALIZED_PHASE_CHANGE (*MAT_254)**. The model was specifically developed for process chain simulations using a consistent material description [4] [5].

The presented work focuses on the numerical simulation of damage evolution in welded joints, under consideration of local phase changes and their underlying properties. The aim was to keep the same material model from welding to loading while considering the effects of local phase transformations for the prediction of damage. To do so, the damage model ***MAT_ADD_GENERALIZED_DAMAGE**, which is a generalized form of ***MAT_ADD_DAMAGE_GISSMO** developed by [6], was adopted. Three optimized sets of parameters of GISSMO, one for each of the three main phases, were identified based on numerical simulations and experimental results using LS-OPT. The approach proposed in [7] reassigns elements to parts characterized by the same mechanical properties after welding. This technique of creating local material clusters was adopted to perform the damage simulation based on the respective present phase of the steel. The three unique sets of parameters were then combined into a multi-phase damage model, which uses a mixing rule to calculate the material properties for arbitrary phase combinations.

For the final damage calculation to verify the correct damage prediction of a welded segment in a three-point bending test, it was realized that the damage model does not work properly in combination with ***MAT_254**. The predicted cracks occurred in an unrealistic manner. Further research must be carried out to determine the exact cause and to fix this problem.

Keywords: GISSMO, MAT_254, multi-phase damage model, welding, Steel C45, phase transformation

METHODOLOGY FOR MULTI-PHASE WELDING SIMULATION

To capture the influence of microstructural phase transformations on damage evolution in the HAZ of structural steel welds, a systematic workflow was established comprising specimen preparation, experimental characterization, material model calibration, and data-field generation for LS-DYNA’s generalized phase-change material (*MAT_GENERALIZED_PHASE_CHANGE*, MAT 254).

Four distinct specimen geometries were manufactured from the same base steel, which was used for the welding task. These geometries were selected to impose varying stress triaxialities during fracture testing. The manufactured specimens were heat treated to create the different phases which are present in the HAZ of the selected base steel.

This results in a suite of specimens representing pure ferrite/pearlite, bainite, and martensite microstructures. Each condition was verified via optical microscopy and image analysis to confirm the expected phases.

The uniaxial stress–strain curves for ferrite/pearlite, bainite, and martensite were each fitted to the piecewise linear plasticity Model (MAT 24). Key parameters (effective plastic strain/yield stress values) were optimized via least-squares matching in LS-OPT. Using the damage model including triaxialities, the GISSMO parameters – triaxial break elongation curve and triaxial material instability curve were calibrated for each phase. The resulting three sets of GISSMO parameters encapsulate the distinct ductile fracture behaviour of each microstructure.

In MAT 254, local phase fractions are provided as state variables at each element. To account for arbitrary mixtures in the HAZ, the single-phase material models must be combined into a continuous material data field. The plastic and fracture responses for the pure phases are tabulated as functions of equivalent plastic strain and stress triaxiality. For any combination of φ_F, φ_B, φ_M (Ferrite, Bainite, Martensite) the resulting effective plastic strain rate as a function of yield stress is already calculated in MAT 254. For the fracture response, the arbitrary combination of the phases needs to be computed by linear equations into a multi-dimensional material map, which returns the material parameters in relation to the triaxiality. This table is then input to MAT 254 via the phase mixture saved for every element in the history variable keyword, enabling on-the-fly evaluation of the mixed-phase mechanical response during welding simulation.

The second approach uses the generalized GISSMO model: MAT_ADD_GENERALIZED_DAMAGE. This model provides up to three history variable which can be addressed each with own GISSMO parameter. This enables to define the GISSMO parameter separated for ferritic-pearlitic phase, bainitic phase and martensitic phase.

MATERIAL PHASES AFTER WELDING

To establish the multi-phase welding simulation, the different material properties for the different phases must be tested. Several phases can form during the welding process, such as upper bainite, lower bainite, martensite or tempered martensite. To keep the simulation complexity manageable, the three main phases ferrite-perlite, bainite and martensite are selected. The material chosen was the normalized structural steel C45, as it is prone to harden after welding due to its higher carbon content. The different phases, which can occur in the heat affected zone are shown in the figure below.

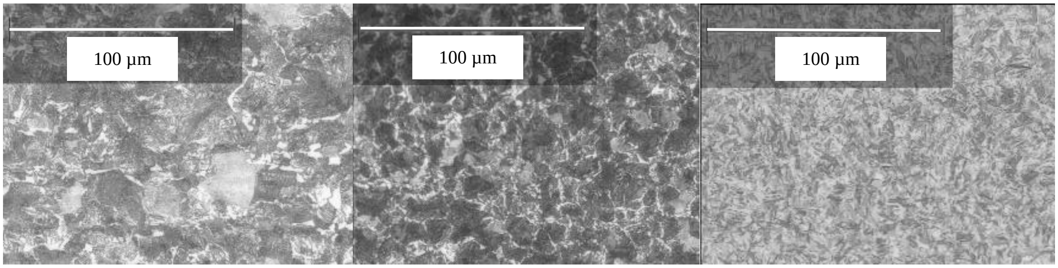

Fig. 1 Different phases of C45 steel of the tensile test specimens. Left: Ferrite-Pearlite, mid: Bainite, right: Martensite

PLASTIC MATERIAL PROPERTIES

The material properties are determined through tensile tests. To obtain phase-specific results, the C45 steel was subjected to various heat treatment processes, during which the three phase-pure microstructures martensite, bainite and ferrite/pearlite were produced. The heat treatment process-parameters are explained in table 1.

Table 1 Heat treatment process-parameters [8]

Heat treatment	Temperature (Austenite)	Cooling
Normalisation	840 °C	Air cooling 20°C
Bainitisation	840 °C	Salt bath 400°C
Hardening	840 °C	Water 20°C

F. X. C. Andrade developed in [9] special triaxial tensile test specimens, which are also used in this study. The geometry of the tensile test specimens and the mount for the tensile testing machine are shown in Fig. 2. The four geometries were modelled in LS-DYNA and boundary conditions were applied just as in the experiment i.e. the keyword *BOUNDARY_PRESCRIBED_MOTION was applied to the inner surface half of the upper hole and the keyword *BOUNDARY_SPC was applied to the inner surface half of the bottom hole with full constraints in all directions. The prescribed displacement was selected according to the respective experiment. The simulation time of the implicit simulation was chosen to be 10 s to ensure no dynamics effects are present. To account for large deformations and stretching of the elements during the simulation, element formulation -2 was used, which corresponds to an 8-point hexahedron element whose algorithm is especially suitable for elements with poor aspect ratio. A mesh size of 0.5 mm was used in the critical area around the crack for each simulation. The meshes are shown below for each specimen.

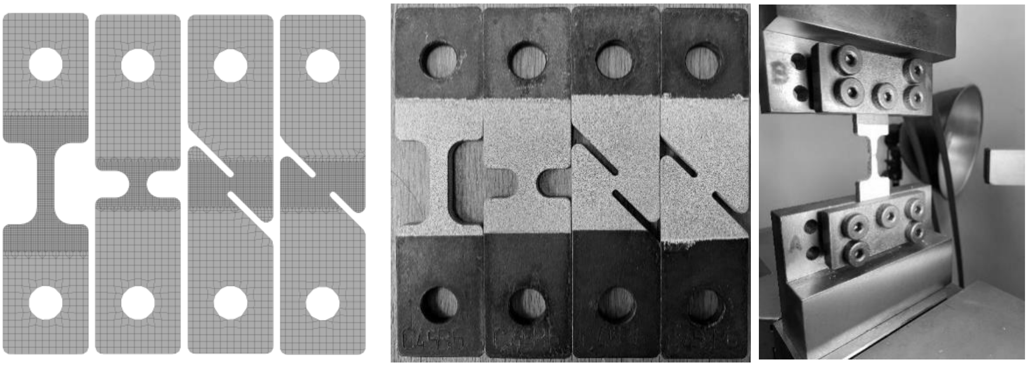

Fig. 2 Different tensile test specimens for different stress triaxialities. Starting from left to right: short specimen, notched specimen, shear 0° specimen and shear 45° specimen

The plastic material behaviour, which is necessary for the material card in LS-DYNA, was identified based on the experimental median curve of the tensile test with the short specimen (see Fig. 2 on the left). The identification of the parameters was done by least-squares matching in LS-OPT. To do so, the post-critical part of the curves was removed. The tensile tests were carried out for each phase and the results for the normalized experiments are shown in Fig. 3. The nominal cross-section area is 25 mm².

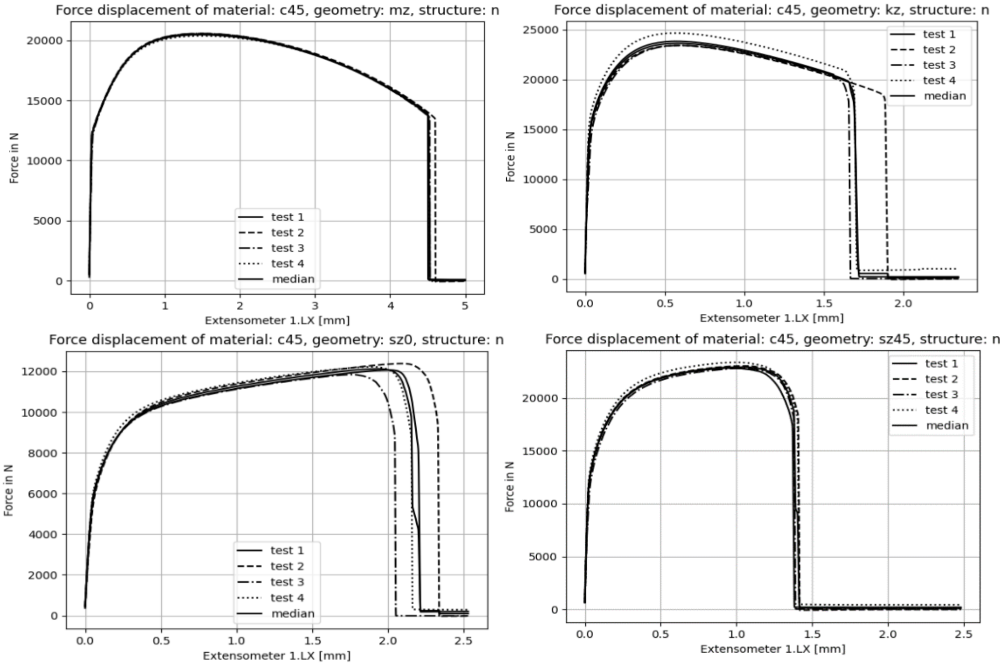

Fig. 3 Force displacement curves for the normalized specimens: short (MZ), notched (KZ), shear 0° (SZ0) and shear 45° (SZ45). For each specimen, four tests were carried out.

For the martensite specimens, the tests could not be evaluated, because their fracture force was not stable. The reason for this behaviour is the brittleness of quenched martensitic steel. After quenching, the specimens were slightly deformed, so they could not be tested without bending stresses. For the novel multiphase fracture model development, the GISSMO model needs especially the plastic behaviour of the material and Martensite has nearly no plastic elongation anymore, so an approximated value for the tensile strength can be used. To test the hardening rate of the material, the formula

$$HV_{max} = 802 \cdot C + 305 \, [C \; in \, \%]$$

can be used to compare the Vickers hardness value with the test specimens [8]. The general behaviour of martensitic steel in relationship to a tempering process of the material is shown in Fig. 4. It becomes clear, that by increasing the tempering temperature, the tensile strength R_m is reduced, and the break elongation A is increased. In the use case of single-layer welding, the tempering process is not present, so the weld seam might have brittle martensitic parts, which can cause cold cracks [10].

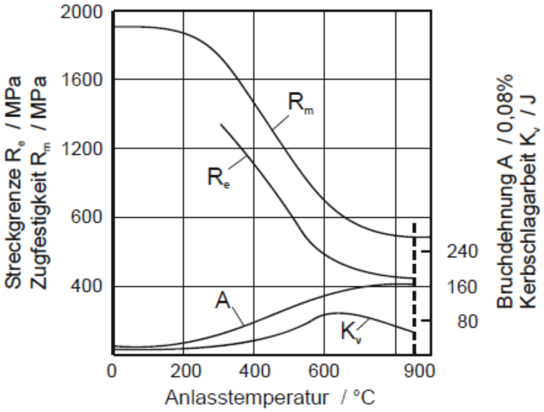

Fig. 4 The material behaviour of martensite before and after tempering [8]

GISSMO DAMAGE MODEL MATERIAL PROPERTIES

The GISSMO Model developed by F. Neukamm [6] was primarily conceptualized for sheet metal forming processes. The advantage of this model is that it defines the failure strain curve and the instability curve as a function of triaxiality, which makes implementation into the simulation easy, if tensile tests of different geometries are available. It is parameterized by the two curves mentioned above as well as by its exponents FADEXP and DMGEXP, where the first one controls the post-critical fadeout of the material and the later one controls the type of damage accumulation e.g. linear or non-linear. The parameters of GISSMO were identified by a multi-objective optimization using LS-OPT. The median experimental curve, including post-critical failure, was matched against the resulting curve of the simulation by using the Genetic Algorithm (GA) in combination with the Leapfrog optimizer (LFOP) to speed up the optimization after a global optimum was found by GA. As an error measure, the mean squared error and curve mapping are available within LS-OPT. The authors of [11], showed that the mean squared error is the superior error measure for this optimization problem and, therefore, it was chosen. The identified fracture and critical strain curves are shown below. For the normalized material, the FADEXP and DMGEXP were identified as 2.0 and 1.6 respectively and for the bainitized material they were identified as 2.0 and 2.5 respectively. For the martenized material, the fracture curve was chosen such that the material is allowed to strain up to 0.5 % plastically. This small amount of plastic strain helped with numerical stability and the location of the crack happened reasonable in the middle of the part. Both damage and fade exponent were taken as 1.0.

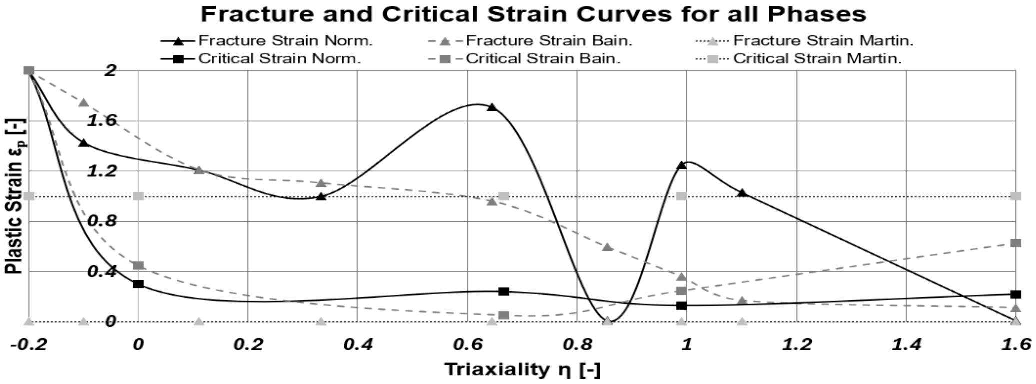

Fig. 6 Fracture and critical strain curves for all three main phases of steel i.e. ferrite/pearlite, bainite, and martensite

Fig. 7 compares experimental curves with simulations, showing good agreement for MZ, KZ, and SZ0 within the experimental scatter (see Fig. 3).

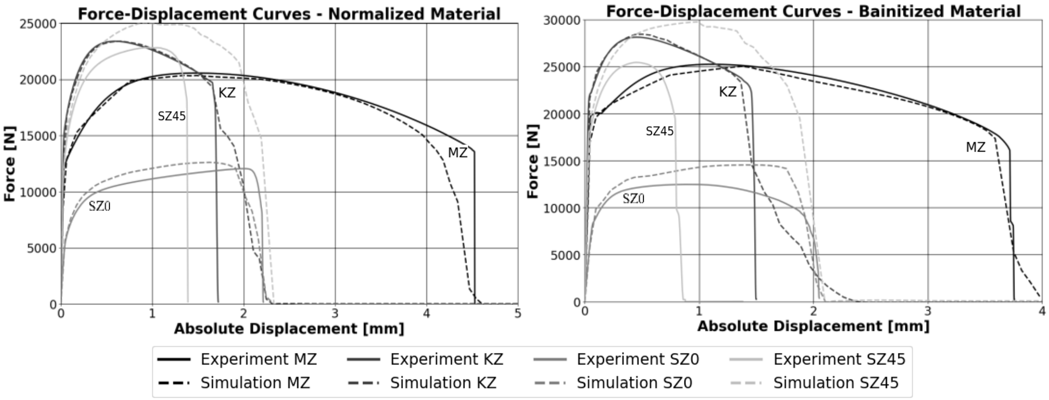

Fig. 7 Force vs. displacement curves for the GISSMO optimization

However, for the SZ45, both the plastic material behavior and the predicted material failure deviate noticeably from the experimental results. The calculated force exceeds the experimentally measured force, which is a phenomenon reported by the authors of [9] as well. The plastic material model *MAT_024 makes use of the J2-based plasticity model which assumes that yielding of the material happens only due to shear stresses. It neglects the influence of hydrostatic stress states. In reality, however, the material is in a complex combination of stresses and the growth of micro defects, due to hydrostatic stresses, might be a reason for the misprediction of the plastic straining. Further research is required to fully understand the underlying process.

In addition to the misprediction of the plastic straining, the GISSMO damage model predicted the failure to be softer and later than in the experiments. To investigate this, the triaxiality and plastic strain of the deleted elements was plotted. For each specimen, the mean curve of the deleted elements was plotted together with the standard deviation from the mean to also visualize the range of triaxiality. The plot shows that the triaxiality of the SZ45 overlaps with the triaxiality of the MZ and KZ specimens, which means that changing the parameters of either MZ or KZ will influence the curve of the SZ45 as well and thus made the optimization difficult.

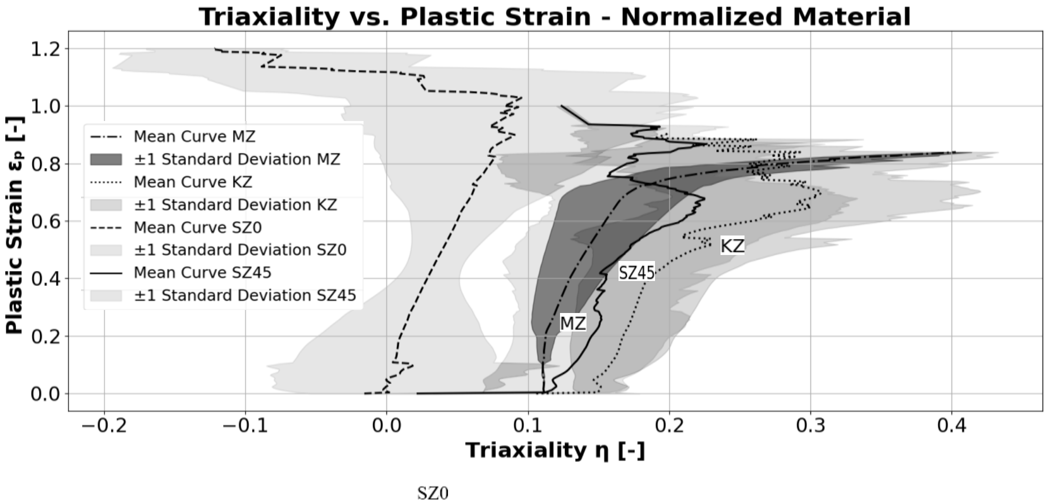

Fig. 8 Triaxiality vs. plastic strain for the normalized material

A visual comparison of the fracture surfaces from the normalized experimental samples and the simulations is presented below. The fracture surfaces for the MZ and KZ specimens were reproduced well by the simulation. For both cases, a smooth crack can be seen.

For the shear specimens, the experimental fracture surfaces appear macroscopically smooth. In contrast, the simulated fracture shows torn elements, leading to an artificially rough surface. This can be attributed to the relatively large mesh size, which is insufficient to resolve microscale fracture mechanisms. A microscopic examination of the experimental surface would likely reveal features more consistent with those observed in the simulation.

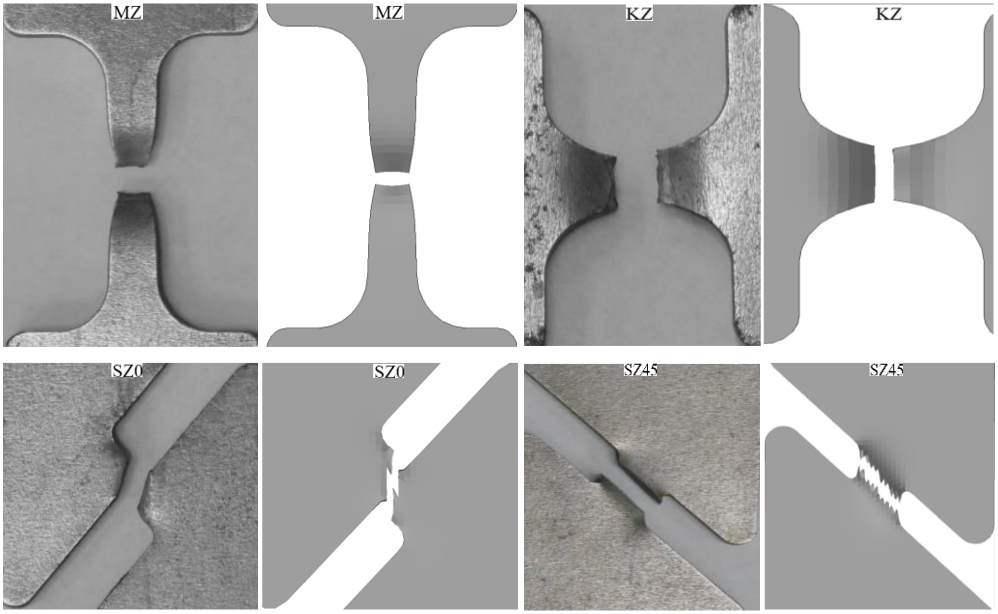

Fig. 8 Comparison of fracture surfaces of experiments vs. simulation

INTERPOLATION OF MATERIAL PROPERTIES WITH LINEAR EQUATIONS

To build the multiphase GISSMO damage model, mainly two curves are necessary to define, the material instability curve ECRIT and the failure curve LCSDG. To calculate the two material curves for every phase combination, a linear system of equations is used to find an explicit description for this problem and the described function ϵ_η solves both curves. These equations are working in two curve definitions in LS-Dyna and calculate the material failure properties for every node as a function of stress triaxiality η. To get the solution parameters a-d for every phase composition, the following linear system of equations must be solved, in which φ_F, φ_B and φ_M are the phase rations of ferrite/perlite, bainite and martensite. The first equation

$$\epsilon_\eta \begin{pmatrix} \varphi_F \\ \varphi_B \\ \varphi_M \end{pmatrix} = a * \varphi_F + b * \varphi_B + c * \varphi_M + d$$

describes a straight line in the $\mathbb{R}^4$ and the second equation

$$\varphi_F + \varphi_B + \varphi_M = 1$$

a plane in the $\mathbb{R}^3$ as a boundary condition, because the phases added up cannot be more than 100%. Only three points are necessary to solve this problem with four unknown variables because of the boundary condition, which cuts the solution plane into a solution line. The three points are already calculated in the GISSMO analysis of the three material simulations with the three different material phases ferrite/perlite, bainite, and martensite. The described solutions

$$\epsilon_\eta \begin{pmatrix}1\\0\\0\end{pmatrix} = LCSDG_{\eta,\varphi_F}, \qquad \epsilon_\eta \begin{pmatrix}0\\1\\0\end{pmatrix} = LCSDG_{\eta,\varphi_B}, \qquad \epsilon_\eta \begin{pmatrix}0\\0\\1\end{pmatrix} = LCSDG_{\eta,\varphi_M}$$

solve the equation ϵ_η for every triaxiality point η of the curves ECRIT and LCSDG and the solutions must be entered into the associated material card.

The second approach uses directly the phase proportion ferrite-pearlite, bainite, and martensite. The material instability curve ECRIT and the failure curve LCSDG are defined separately for each phase. The damage index is calculated according to these parameters weighted by the phase proportion.

MICROSTRUCTURE SIMULATION AND SOURCE DATA

The LS-DYNA Material Model *MAT_GENERALIZED_PHASE_CHANGE (*MAT_254) supports different models to calculate the phase transformation. For this investigation the Koistinen-Marburger Law is applied for the diffusion-free Austenite-Martensite transformation. The decomposition from Austenite to Bainite and Ferrite-Pearlite is calculated with the generalized Johnson-Mehl-Avrami-Kolmogorov model (JMAK). In welding tasks, the cooling is continuous and does not contain any hold times. The transformation is described by Constant-Cooling-Time (CCT) diagrams. The phase proportion at complete cooling is defined by cooling time needed for the temperature-interval between 800 °C and 500 °C. The value for PEQ TAU and N of the JMAK model are kept constant and the Leblond parameter F which describes the transformation velocity depending on the cooling rate is used to adjust the phase transformation. For this work the source data for the phase transformation is taken from WeldWare® [12] [13]. The data based on many physical experiments known as physical welding simulation performed by Seyffarth, Groß and Scharff and published in [14]. WeldWare® provides the data for phase transformation from Austenitisation at 1350 °C down to complete cooling according the cooling time between 850 °C and 500 °C. The chemical composition for the Steel C45 used in this work is given in Table 2.

Table 2 Chemical Composition C45 in wt. %

C	Si	Mn	P	S	Cr	Ni	Mo	Cu	Al	Ti	Nb	N
0,47	0,24	0,68	0,01	0,001	0,22	0,02	0,004	0,01	0,022	0,003	0,001	0,004

A simple model of single independent cube is used to check phase transformation. At each cube a thermal cycle with constant cooling rate is applied. Fig. 9 shows the phase – cooling time – transformation diagram with source data from WeldWare® and the result from simulation check.

In addition, the yield stress, tensile stress, elongation at break and hardness for uniaxial tensile test are provided by Weldware® according the cooling time.

*MAT_GENERALIZED_PHASE_CHANGE (*MAT_254) provides eight history variables, which can be defined by user defined functions. This enables the output of the mechanical properties after change of microstructure. Fig. 10 shows the yield stress and tensile stress over cooling time. Fig. 11 shows the elongation at break over cooling time. Both diagrams point out that the source data is hit exactly by the simulation approach.

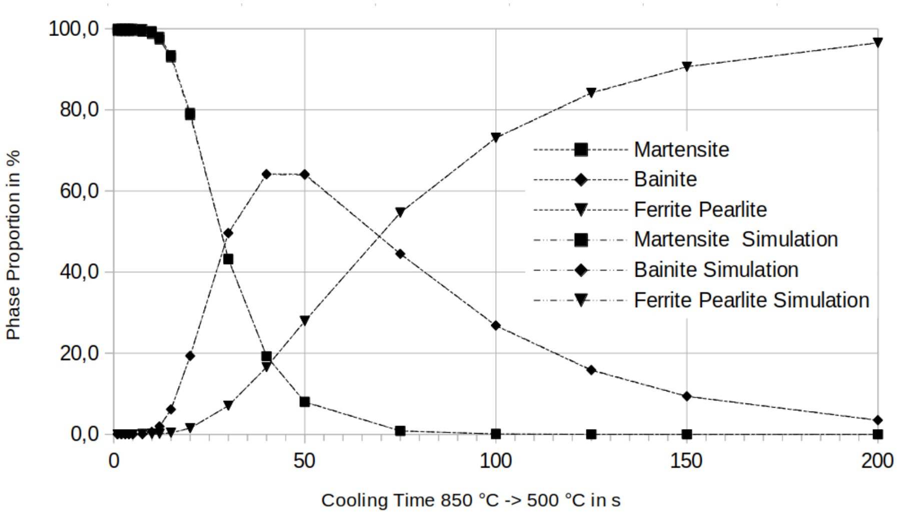

Fig. 9 Phase Proportion over Cooling Time; Source data vs. simulation

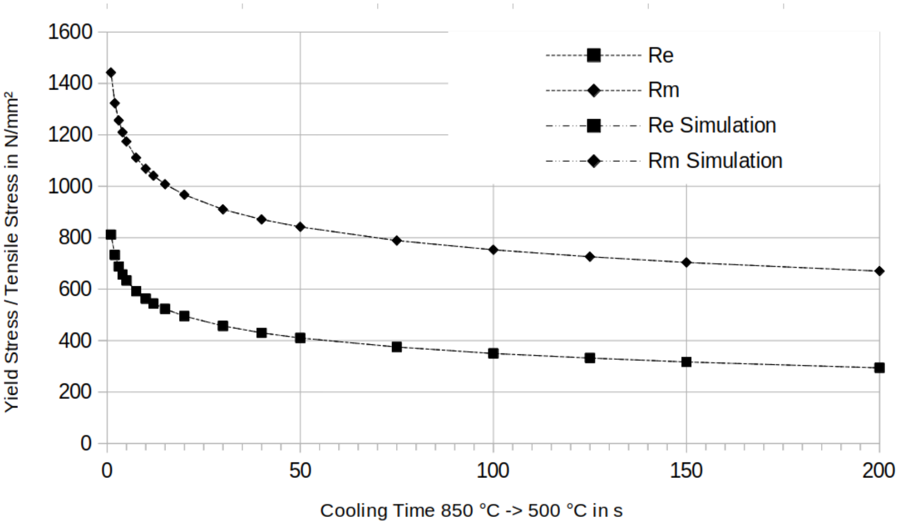

Fig. 10 Phase Proportion over Cooling Time; Source data vs. simulation

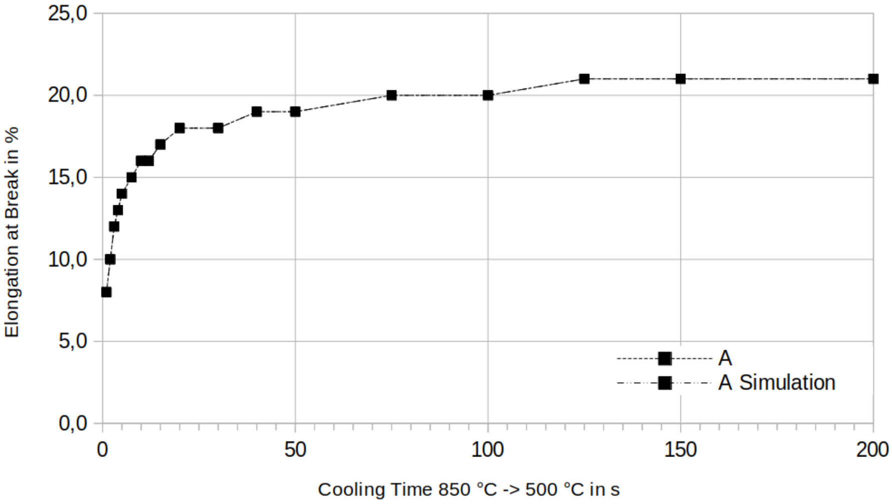

Fig. 11 Phase Proportion over Cooling Time; Source data vs. simulation

The use of WeldWare® data enables engineering in advance without any physical material testing. In this work, tensile test of the material was performed for base material (normalized), bainitic microstructure and martensitic microstructure. As a result, a difference between tensile tests of the chosen material and WeldWare® data can be seen. The mechanical properties and flow curve data from tensile tests are applied in the material model used for the simulations.

EXPERIMENTAL VALIDATION OF THE DAMAGE MODEL

In order to validate the predictive capability of the proposed damage model for simulated weld seam strength and fracture behaviour, a series of TIG (Tungsten Inert Gas) welding specimens were produced and mechanically tested with a three-point bending experiment. This chapter details the welding parameters, specimen geometry, testing procedure, and observed results for both top-side and bottom-side bending tests.

WELDING PROCEDURE

All specimens were produced as blind butt welds in 5 mm thick plates of the selected structural steel. An argon-shielded TIG process was employed with the following nominal parameters:

- Current: 300 A; Voltage: 13 V; Welding Speed: 5 mm/s
- Shielding gas: Argon; flow: 15 L/min
- Joint type: Blind weld (no full penetration)

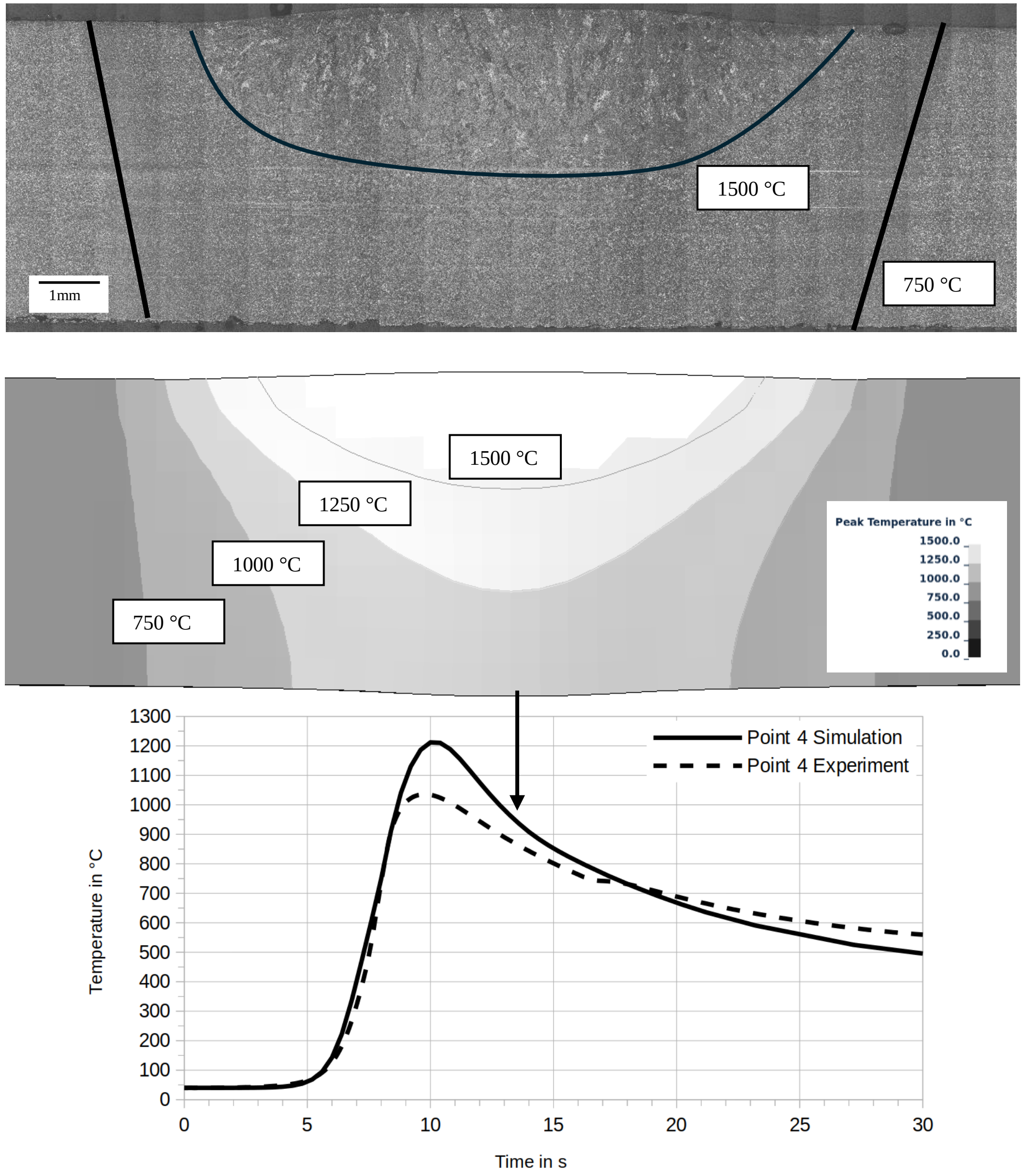

Fig. 12 Macro section of welding and cross-section with peak-temperature of simulation. The HAZ lines are thick black and the solidification lines are thin black. The temperature progression was measured with TC on the bottom side of the welding seam.

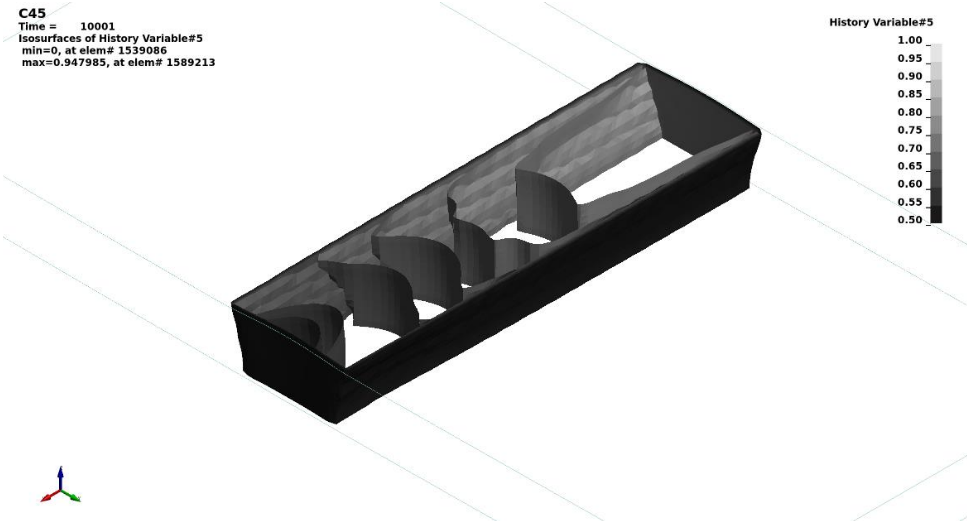

Fig. 13 Martensite proportion

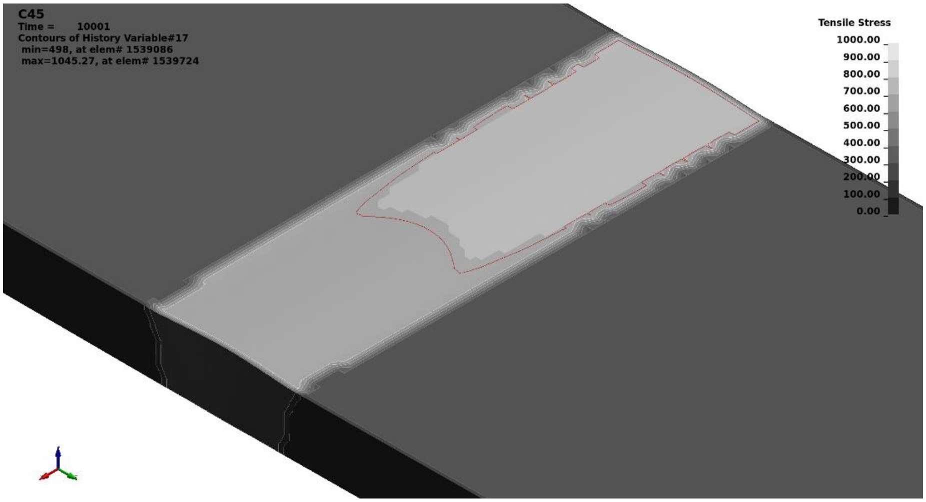

Fig. 14 Tensile stress after welding according to WeldWare® data

Prior to welding, joint faces were prepared by manual grinding to a clean surface. The root side remained unwelded to simulate a common partial-penetration condition. Each weld pass was executed with no filler material added in the root region to ensure consistent lack of penetration and no material mixing.

After welding, specimens were allowed to cool to ambient temperature under still-air conditions. The resulting macro section of weld experiment, compared with the peak temperature of the simulation are shown in Fig. 12 and show a good accordance. The temperature over time at bottom side in the centerline measured by thermocouple is also in good accordance with the result of the simulation (Fig. 12).

After welding the plate is cut to the size of specimen for the bending test. The cutting is also considered in the simulation by erasing all elements outside the test specimen.

One result of the simulation is the phase composition of the microstructure. Fig. 13 shows the martensite proportion after welding. The faster cooling at begin of the weld leads to higher martensite composition than at end of the weld.

Fig. 14 displays the tensile stress computed by evaluating the cooling time according to the data provided by WeldWare®.

THREE-POINT BENDING TEST SETUP

Mechanical validation was performed according to DIN EN ISO 5173 (“Bend Test”) in an universal testing machine. Specimens were machined into rectangular cross-sectional bars (dimensions: 95 mm × 40 mm × 5 mm), with the weld seam running longitudinally at mid-span. Four specimens were tested with the weld crown facing upward (top-side bending) and four with the weld root facing upward (bottom-side bending). During each test, load–deflection curves were recorded continuously.

FIRST RESULTS

All four top-side specimens exhibited brittle fracture initiating at the weld centerline. The maximum bending load averaged was 19.4 kN. The fracture surfaces exhibit a brittle fracture pattern that continues centrally within the weld seam. The crack-pattern of the top-side specimens are shown in Fig. 15.

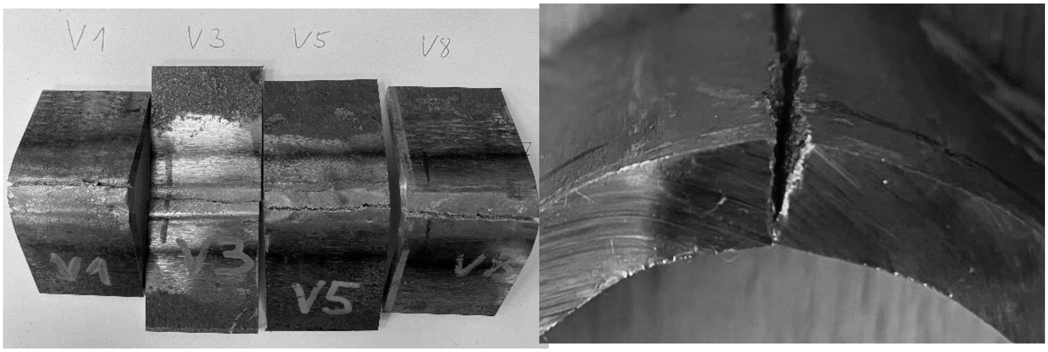

Fig. 15 Fracture pattern of the top-side specimens with martensitic brittle fracture pattern

In contrast, none of the four bottom-side specimens fractured under the same loading conditions, as shown in Fig. 16.

Fig. 16 Bottom-side specimens with no fracture after testing. The plastic flow of material around the HAZ is observed.

Instead, the specimens exhibited continuous plastic deformation around the heat-affected zone (HAZ), with material bulging and flowing into the unwelded root gap. Maximum loads reached up to 21.5 kN without any macroscopic crack formation. The described behaviour of the two different tests is shown in the force displacement curves in Fig. 17. The ductile behaviour of the bottom-side of the welding seam confirms that the absence of full penetration allows stress redistribution, preventing critical damage accumulation as described by the model.

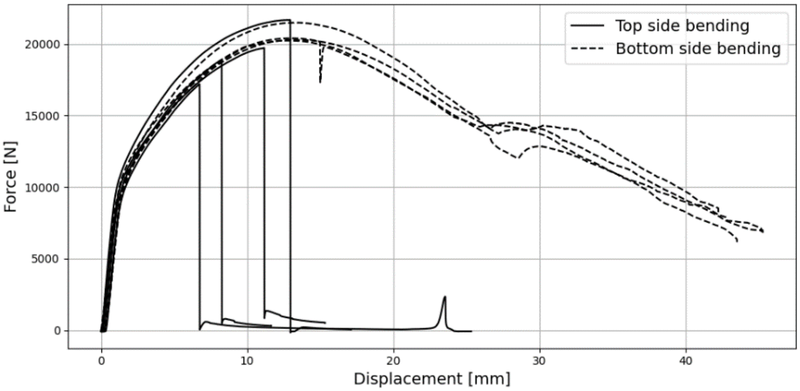

Fig. 17 Force displacement curves of the bending test. Left: top-side, right: bottom-side

Next step is the simulation of bending test with correct detection of fracture. It will be evaluated which of the both approaches for the damage model fits better the real experiment.

CONCLUSION

In this study, a methodology for mixing rules for the mechanical properties of different phases in steel was successfully demonstrated. The approach considers both, elastic-plastic behaviour and damage properties. This was made possible through single-phase, standardized tensile specimens that represent the distinct mechanical characteristics of the steel microstructures.

Based on the proposed linearized mixing rule, the mechanical properties of phase mixtures present in the heat-affected zone of welded joints were subsequently determined. Experimental three-point bending tests provided a basis for validating the developed simulation model.

A final validation has not yet been completed at the time of publication, as errors occur in the applied GISSMO implementation in LS-DYNA in combination with the multiphase material model MAT254. Furthermore, the developed methodology is currently limited to welding processes without filler materials. Additional research is required to incorporate filler metals by accounting for the dynamic melt mixing driven by electromagnetic forces, thereby enabling the consideration of locally evolving alloy compositions and their influence on mechanical properties.

References

[1] T. LOOSE: *Einfluß des transienten Schweißvorganges auf Verzug, Eigenspannungen und Stabilitäsverhalten axial gedrückter Kreiszylinderschalen aus Stahl*, 2007.

[2] J. HILDEBRAND: *Numerische Schweißsimulation Bestimmung von Temperatur, Gefüge und Eigenspannung an Schweißverbindungen aus Stahl- und Glaswerkstoffen*, 2008.

[3 T. LOOSE and T. KLOEPPEL: *An LS-DYNA material model for the consistent simulation of welding, forming and heat treatment*, 2015.

[4] T. KLÖPPEL, A. ERHART, A. HAUFE and T. LOOSE: 'Recent Developments in LS-DYNA to close the virtual process chain for forming, press hardening and welding', *18th Internationals Esaform Conference on Metal Forming*, 15. - 17. April 2015, Graz, Austria.

[5] T. LOOSE, J. R. J. PREHM and U. DIEKMANN: *Simulation chain of material simulation, heat treatment simulation and welding simulation for industrial application*, 2018.

[6] F. NEUKAMM: *Lokalisierung und Versagen von Blechstrukturen*, 2018.

[7] J. PREHM and T. LOOSE: *Determination of weld joint strength by welding simulation*, 2019.

[8] E. ROOS and K. MAILE: *Werkstoffkunde für Ingenieure*, Springer, 2015.

[9] C. ANDRADE, M. FEUCHT, A. HAUFE and F. NEUKAMM: *An incremental stress state dependent damage model for ductile failure prediction*, CrossMark, 2016.

[10] G. SCHULZE: *Die Metallurgie des Schweißens*, Heidelberg: Springer, 2010.

[11] J. EFFELSBERG and M. FEUCHT: *Identifikation von Materialparametern mit LS-OPT - GISSMO und andere Anwendungen*, 2014.

[12] A. SCHARFF and C. KÖTHE: 'Ermittlung der mechanischen Kennwerte von MAG-Schweißgut mit Hilfe des schweißtechnologischen Beratungssystems WeldWare®', *DVS-Berichte, vol. 156, pp. 102-156, 1993*.

[13] A. SCHARFF: 'WeldWare® - the weldability of steel-based materials', IN *Computer in Welding Education & Engineering, Stockholm*, 1995.

[14] P. SEYFFARTH, B. MEYER and A. SCHARFF: *Großer Atlas Schweiß-ZTU-Schaubilder*, Düsseldorf: DVS-Verlag, 1992.